Supplementary Information for

Tunable Berry curvature and transport crossover in topological Dirac semimetal KZnBi

Junseong Song[1,2†], Byung Cheol Park[1†], Kyung Ik Sim[2], Joonho Bang[1], Sunghun Kim[3], Zhuo Yang[4], Yoshimitsu Kohama[4], Yeongkwan Kim[3,5], Sung Wng Kim[1,2,*]

[1]Department of Energy Science, Sungkyunkwan University, Suwon 16419, Republic of Korea.

[2]Center for Integrated Nanostructure Physics, Institute for Basic Science, Suwon 16419, Republic of Korea.

[3]Department of Physics, Korea Advanced Institute of Science and Technology, Daejeon 34141, Republic of Korea.

[4]Institute for Solid State Physics, The University of Tokyo, Kashiwa, Chiba 277-8581, Japan.

[5]Graduate School of Nanoscience and Technology, Korea Advanced Institute of Science and Technology, Daejeon 34141, Republic of Korea.

[†]These authors contributed equally to this work.

*Corresponding author: kimsungwng@skku.edu

This Supplementary Information includes:

Supplementary Figures 1–8

Supplementary Tables 1 and 2

Supplementary Figures and Tables

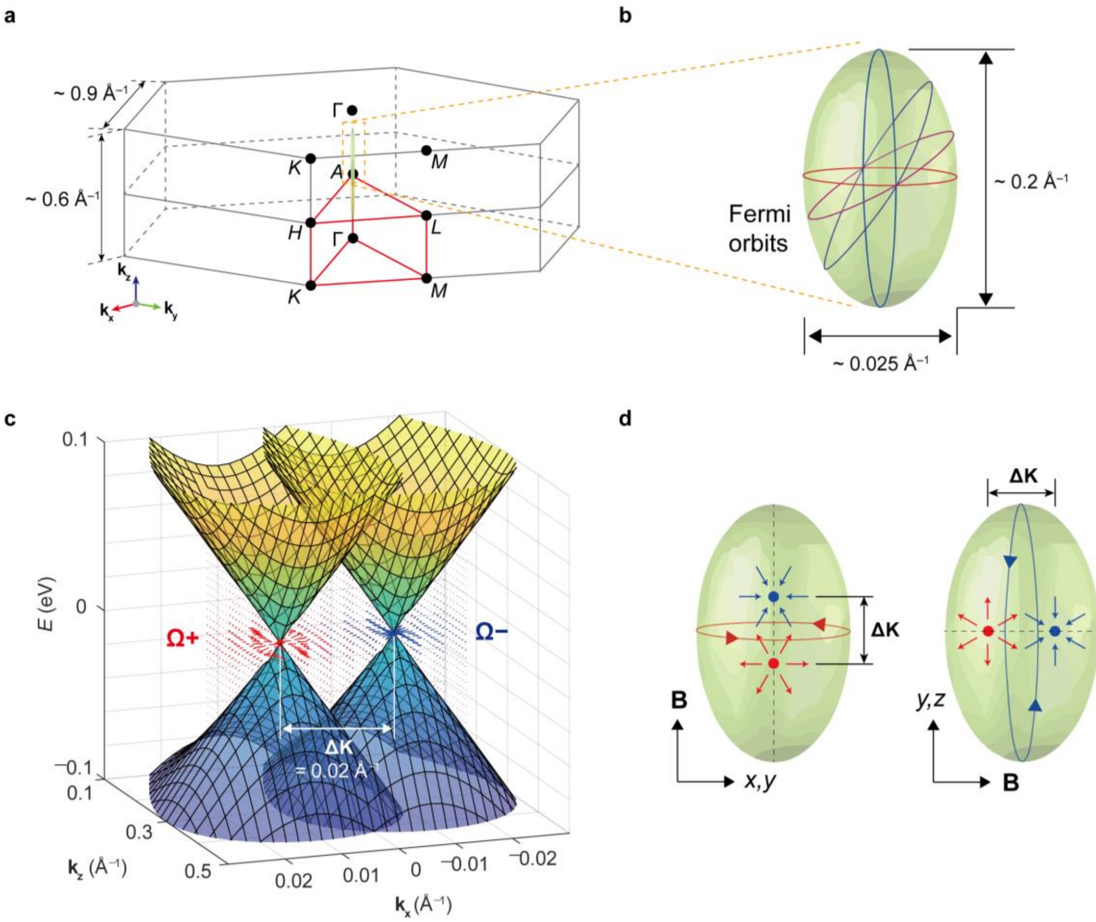

Supplementary Fig. 1 | Calculation of Berry curvature (Ω±) distribution for the 3D TDS KZnBi under the magnetic field (B) and estimation of its effect on the magneto-transport properties. a, The first Brillouin zone (BZ) obtained from the crystal structure through the relation between real and reciprocal space. The elongated Fermi surface is lying along the Γ–*A*–Γ direction. **b**, Fermi surface geometry and Fermi orbits for Dirac fermions acquired from the angle-dependent MR data. **c**, Berry curvature distribution of the KZnBi in the BZ. The source (**Ω**+) and sink (**Ω–**) of the Berry curvature are located at the Weyl nodes, which are split from a single Dirac node due to the **B**. The separation (**ΔK**) between Weyl nodes was obtained from the AH conductivity analysis (see text). The dispersion of the Weyl cones was determined based on both the ARPES data in ref. 17 and our magneto-transport properties. **d**, The estimation of Weyl node splitting and Fermi orbit, which relies on the direction of **B**. The Berry flux piercing through the Fermi orbit determines the size of Berry curvature. Note that the direction of the dipolar Berry field is always perpendicular to that of the orbital motion of fermions.

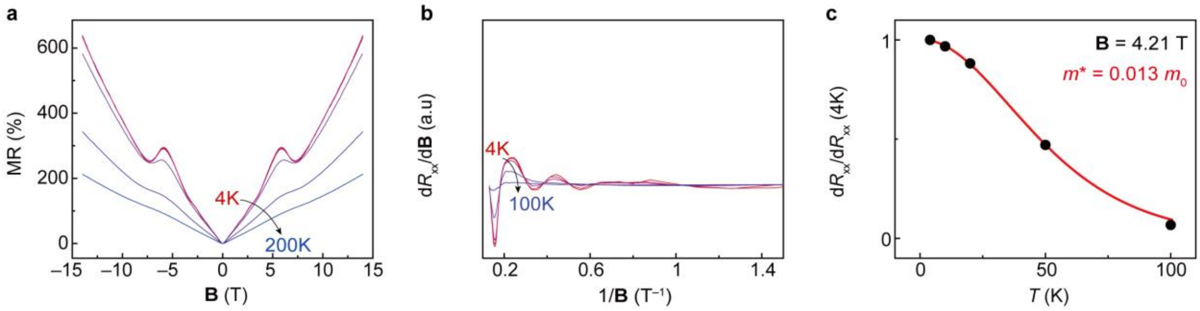

Supplementary Fig. 2 | Magneto-transport measurement data of sample 2 (E_F = −85.1 meV). a, MR under −14 T ≤ **B** ≤ 14 T at T = 4 K (red), 10K, 20 K, 50 K, 100 K, 200 K (blue). **b,** SdH oscillation component in dR_{xx}/d**B** as function of 1/**B** at the same T. **c,** T-dependent experimental SdH oscillation amplitudes (dots) at **B** = 4.21 T and fitting line (red curve) with Lifshitz-Kosevich formula to obtain the effective mass $m^* \cong 0.013\ m_0$. Please see Supplementary Table 1 for all physical parameters.

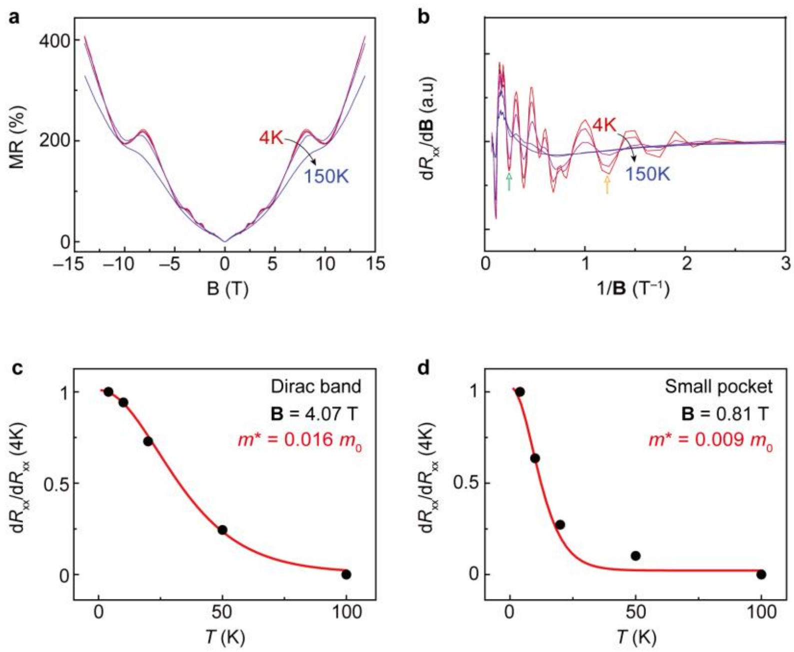

Supplementary Fig. 3 | Magneto-transport properties of sample 3 (E_F = −102.6 meV). a, MR under −14 T ≤ **B** ≤ 14 T at T = 4 K (red), 10K, 20 K, 50 K, 100 K, 150 K (blue). **b,** SdH oscillation component as function of 1/**B** at the same T. Two oscillatory components, which were attributed to the Dirac band (green arrow) and and small pocket (orange arrow) based on two-carrier analysis and DFT calculation results[17]. **c,** Experimental SdH oscillation amplitudes (dots) for the Dirac band at B = 4.21 T (green arrow in **b**) and fitting line (red line) giving effective mass $m^* \cong 0.016\ m_0$. **d**, T-dependent SdH oscillation amplitudes (dots) for the small pocket at B = 0.81 T (orange arrow in **b**) and fitting line (red line) giving $m^* \cong 0.009\ m_0$. Please see Supplementary Table 1 for all physical parameters.

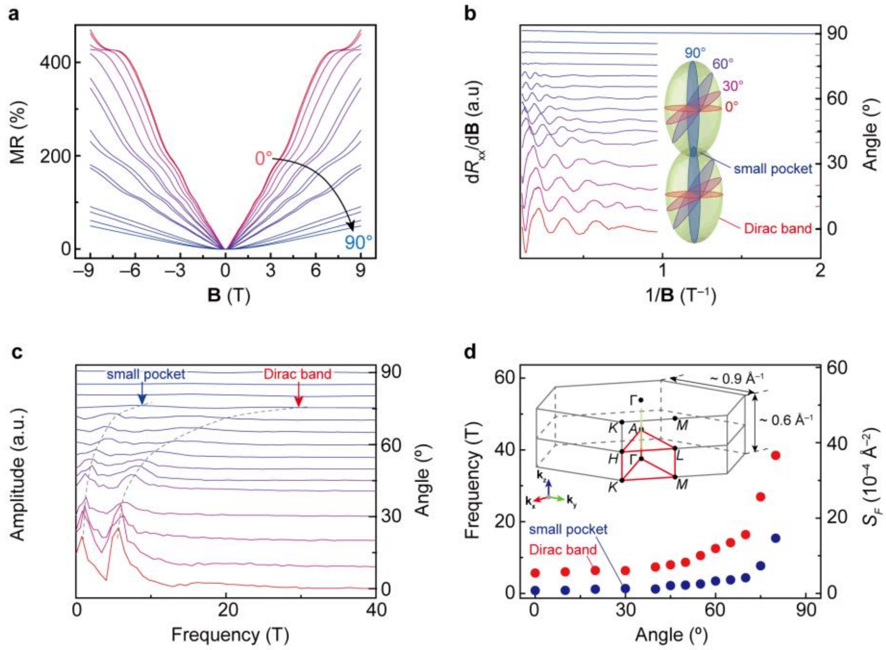

Supplementary Fig. 4 | The analysis of angle-dependent MR of sample 4, whose band structure contains both Dirac band and small pocket at E_F = –91.1 meV. a, θ-dependence of MR under -14 T ≤ **B** ≤ 14 T at T = 4 K. **b,** SdH oscillations in dR_{xx}/d**B** as a function of 1/**B** at given θ values (right axis). Inset shows a schematic illustration of the Fermi surface (green ellipsoids) and its cross-sections (color areas) for directions of the **B** field. **c,** Fast Fourier transformation of SdH oscillations in **b** gives two peaks (dashed lines) at two different frequencies. The Dirac band at higher frequency and the small pocket at lower frequency. **d,** θ-dependence of the oscillation frequencies (left axis) and corresponding Fermi surface area, S_F (right axis) for Dirac band (red balls) and small pocket (blue balls). Inset shows the Fermi surface constructed by collecting the θ-dependent S_F inside the Brillouin zone on the central line along the Γ–A– Γ direction.

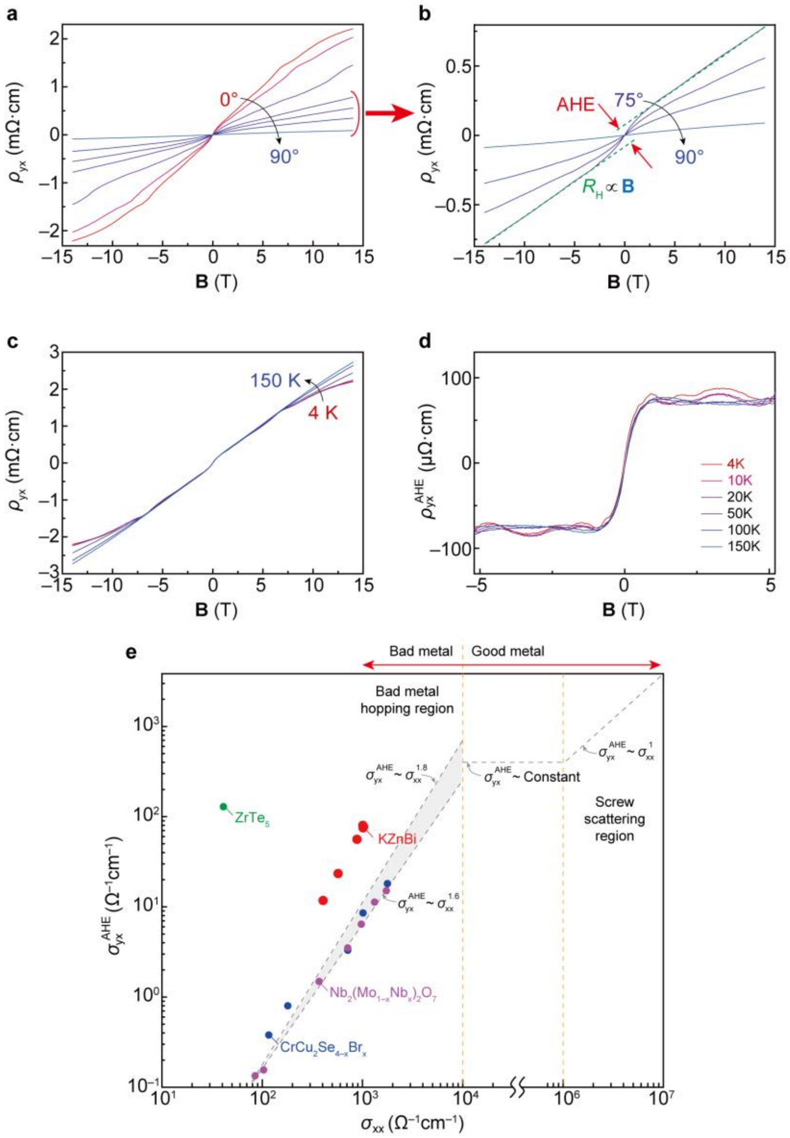

Supplementary Fig. 5 | θ-dependence of Hall resistivity. a, Hall resistivity data at $0° \leq \theta \leq 90°$ in the range of -14 T $\leq$ **B** $\leq$ 14 T. **b,** Enlarged view of Hall resistivity data for θ between 75° and 90°. AHE contributions are separated by subtracting the ordinary Hall contribution, R_H. **c**, Temperature-dependent Hall resistivity data at 4 K $\leq T \leq$ 150 K in the range of -14 T $\leq$ B $\leq$ 14 T. **d**, AH resistivity values extracted from the temperature-dependent Hall resistivity data in **c**. **e,** Scaling plot between AH conductivity (σ_{yx}^{AHE}) and longitudinal conductivity (σ_{xx}) for the KZnBi in comparison with other materials.

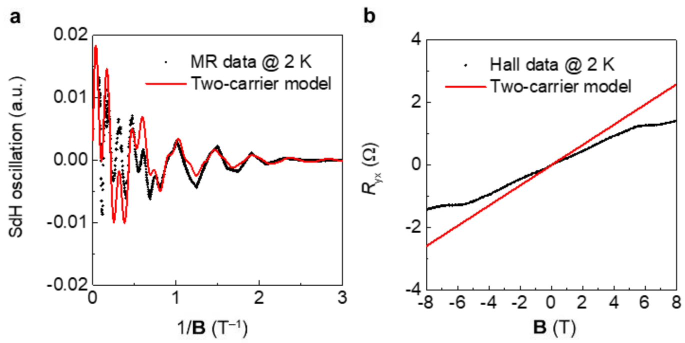

Supplementary Fig. 6 | Two-carrier model, which is proper for the SdH oscillation analysis but, is not suitable for interpreting the nonlinearity of the Hall signal. a, Two-carrier model fitting to SdH oscillations. Physical parameters are extracted from the analysis (see text). Dots are the experimental data and red line is a fitting line. **b**, AH resistance of the KZnBi, which is inconsistent with two-carrier model.

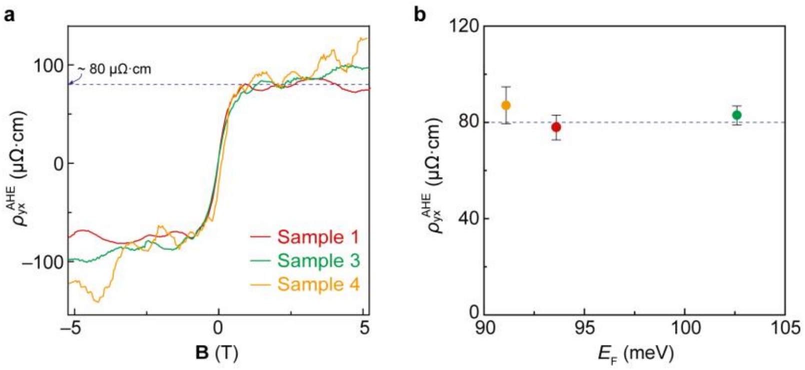

Supplementary Fig. 7 | AH resistivity data, $\boldsymbol{\rho_{yx}^{\mathrm{AHE}}}$, of the KZnBi samples, which are independent on the $\boldsymbol{E_F}$ position. a, Raw ρ_{yx}^{AHE} data for three different samples with different E_F values and **b**, the saturation values of ρ_{yx}^{AHE} are nearly constant over E_F in the KZnBi, supporting the Berry curvature origin of ρ_{yx}^{AHE}.

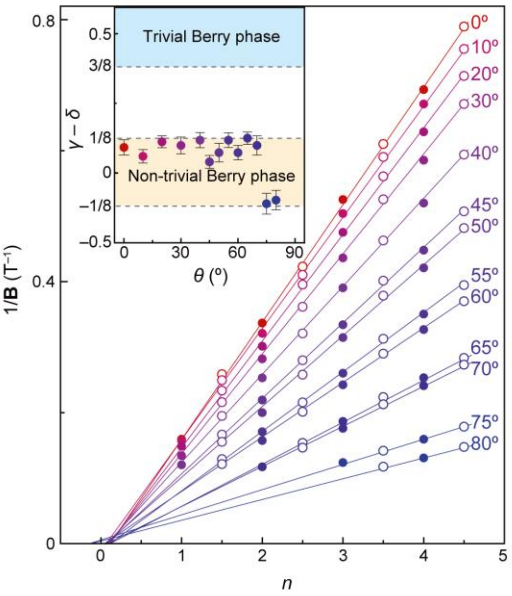

Supplementary Fig. 8 | Non-trivial Berry phase for all *θ*. —θ-dependence of Landau fan diagram (1/**B** versus n) for sample 4. The maxima and minima of SdH oscillations were assigned to integer indices (filled circles) and half-integer indices (open circles) of the Landau levels, respectively. The intercept values of $|\gamma - \delta|$ for all θ are lying between 0 and 1/8, implying the presence of the non-trivial Berry phase and, therefore, the absence of the topological phase transition (inset). The error bar is 95% of confidence intervals. The sign change at the critical angle ~70º can be explained with the anisotropic geometry of the Fermi surface, where the orbit of Dirac fermions cannot involve a perfect π Berry phase [27].

Supplementary Table 1 | Summary of the physical parameters of sample 1 to 4

Sample	m^* (m_0)	d(1/**B**) (T^{-1})	S_F (10^{-4} Å^{-2})	$\mathbf{k_F}$ (Å^{-1})	v_F (10^6 m·s^{-1})	E_F (meV)
1	0.012	0.213	4.6	0.012	1.19	93.6
2	0.013	0.209	4.56	0.012	1.07	85.1
3	0.016	0.141	6.81	0.015	1.04	102.6
4	0.014	0.184	5.43	0.013	1.08	91.1

Supplementary Table 2 | Transport properties of reported Dirac and Weyl semimetals. The magnetic field at the upturn, a critical field $\mathbf{B}_c$ (T), is compared.

Material	$\mathbf{B}_c$ (T)	μ_H ($cm^2V^{-1}s^{-1}$)	MR (%)	E_F (meV)	NMR (%)	m^* (m_0)	Ref.
Na_3Bi	5	2600	450	29	−75	-	8
$ZrTe_5$	~8	-	~7000	Close to Dirac point	−80	0.03	14
TaAs	5	163000	80000	-	−0.3	-	28
TaAs	0.5	~400000	~600000	-	−1~−3	-	29
Cd_3As_2	3-7	-	~80	~54	−60	-	30
Cd_3As_2	9	~11000	100	-	−60	-	13
Cd_3As_2	2	~15200	1500	-	−7	-	31
KZnBi	~0.2		~700	93.6	−0.3	0.012	This work